Supporting Information

Lysozyme-Templated Meso-Macroporous Hollow TiO_2 for Lithium-Ion Battery Anode

Muhammad Saad Salman,[†,∥] A Reum Park,[†,∥] Min Jin Cha,[‡] Youngjin Choi,[†] Sung Kyu Jang,[‡] Lihan Tan,[*,§] Pil J. Yoo,[*,†,‡] and Woo-Seok Choe[*,†,‡]

[†] School of Chemical Engineering and [‡] SKKU Advanced Institute of Nanotechnology, Sungkyunkwan University, Suwon 16419, Republic of Korea

[§] A*STAR, Downstream Processing Group, Bioprocessing Technology Institute, 20 Biopolis Way, Centros #06-01, Singapore 138668, Singapore

* E-mail: tan_lihan@bti.a-star.edu.sg (Lihan Tan), pjyoo@skku.edu (Pil J. Yoo) and checws@skku.edu (Woo-Seok Choe)

The Supporting Information consists of the following:

Experimental details

Figures: S1-7

Tables: Table S1

EXPERIMENTAL DETAILS

Materials

Lysozyme from chicken egg white, titanium (IV) bis(ammonium lactato) dihydroxide (TiBALDH) and trifluoroacetic acid (TFA) from Sigma-Aldrich (USA), dipotassium hydrogen phosphate from Junsei (Japan), 1,4-dithiothreitol (DTT) from Ameresco (USA), and acetonitrile (ACN) from Daejung Chemical (Korea) were purchased. Purified water obtained from a water purification system (Arium 611VF, Sartorius-Stedim, Germany) was used in the experiments.

Preparation of native and denatured lysozyme biotemplates

Native lysozyme solutions (N, NP) were prepared in water or 50 mM phosphate buffer (PB) at pH 8, respectively, to give a solution of 3 mg mL^{-1} lysozyme. The denatured lysozyme solutions (D, DP) were prepared by the addition of 4 mM of DTT to the native lysozyme solutions in water or PB, respectively, followed by heating at 80 ^{o}C for 1 h.

Synthesis of lysozyme-templated TiO_2 particles

For TiO_2 biomineralization, 900 μl of a protein solution prepared as above was incubated with 100 μL of 1 M TiBALDH precursor on a mixer (SLRM-2 M, Seoulin Bioscience, Korea) at 30 rpm, 25 ^{o}C for 15 min. The TiO_2 particles (TN, TNP, TD and TDP) were then collected by centrifugal separation (5804 R, Eppendorf, Germany) at 13000 *g* for 5 min. In order to remove excess TiBALDH precursor, the TiO_2 particles thus obtained in the form of pellet were washed twice each with ethanol and water. Subsequently, the TiO_2 particles were resuspended in the water and freeze-dried (FDU-1200, EYELA, Japan).

Characterizations of lysozyme biotemplates and TiO_2 particles

The degree of lysozyme biotemplate denaturation was determined by high-performance liquid chromatography (HPLC) system (2998 PDA detector, 1525 binary HPLC pump, Waters, USA)

using a Jupiter 5 μm C5 300 Å reversed-phase (RP) column (150×4.60 mm, Phenomenex, Aschaffenburg, Germany). In brief, ACN and water with 0.1% (v/v) TFA were used for gradient elution from 34 to 46% (v/v) of ACN at a flow rate of 1 mL min^{-1}. All samples were filtered with cellulose acetate 0.2 μm filter before sample injection. UV-Vis analysis of the biotemplates was performed on a UV-Vis spectrophotometer (Multiskan GO, Thermo Fisher Scientific, USA) in the respective buffers.

The morphology and size of the biotemplates, and TiO_2 particles were analyzed by Field Emission Scanning Electron Microscopy (JEOL-JSM7500F FESEM, Japan) and Transmission Electron Microscopy (JEOL-JEM-2100F TEM). For FESEM analysis, freeze-dried TiO_2 samples were dispersed in DI water ultrasonically (ElmaSonic P, 30 kHz, Elma Schmidbauer GmbH, Germany). A tenfold diluted sample suspension was then dropped onto the pre-cleaned silicon wafer, air-dried, and coated by platinum sputter before analysis. For TEM and EDX analysis, a twenty-fivefold diluted sample suspension was deposited on a carbon-coated 200 mesh Cu grid. Lysozyme solutions (for soluble biotemplates, i.e., N, NP and D) were negatively stained with 2% (w/v) uranyl formate for 1 min. The excess liquid on the grid was wicked off using filter paper, and the grid was air-dried before TEM analysis. For the liquid mode AFM, 5 μL of a biotemplate was pipetted onto the mica substrate, and a few μL of water or PB was dispensed into the silicon nitride AFM tip (Veeco Inc., USA). The AFM images were obtained on a Digital Instruments Nanoscope III (Vecco Inc.) with a multimode fluid cell head in the tapping mode under water or PB.

X-ray diffraction (XRD) of calcined TiO_2 samples (500, 700 or 800 ^oC for 2 h) was carried out on a Bruker D8 Advance diffractometer using the Cu Kα (40 kV, 40 mA), and data were acquired from a 2θ range of 20 to 70° at a step size of 0.02° s^{-1}. The pore diameter and volume of

calcined TiO_2 samples (500 or 700 ºC for 2 h) were measured by Brunauer-Emmett-Teller (BET) surface area measurement analyzer (ASAP 2000, Micromeritics Instrument Corporation, USA). Thermogravimetric analysis (TGA) of TiO_2 samples was performed on a thermogravimetric analysis system (Exstar 6000 TG/DTA6100, Seiko, Japan) by heating from 25 to 800 °C at a rate of 10 °C min^{-1} in air atmosphere. For calcination, TiO_2 samples were first preheated at 300 °C for 1 h, calcined at 500 ºC for 2 h, and then further calcined at the temperatures of either 500 or 700 °C for 2 h in a box furnace. In addition, the elemental composition of calcined TiO_2 samples (700 ºC for 2 h) was analyzed by X-ray Photoelectron Spectrophotometer (XPS) (ESCALAB 250, Thermo Fisher Scientific), where the X-ray source was Al Kα and the reference C 1s was at ca. 284.5 eV (with correction error of ± 0.6 eV).

Electrochemical characterizations of TiO_2 particles

All electrochemical measurements were carried out on CR2032 coin cells. TiO_2 samples were mixed with conductive black (Super-P) and polyvinylidene fluoride (PVDF) in N-methyl-2-pyrrolidone (NMP) at 8:1:1 (w/w) to form a homogeneous slurry. The slurry was uniformly applied to the Cu foil to achieve ca. 1.6 mg cm^{-2} of an active mass with a film thickness of 20 μm. Coin cells were then assembled inside an argon-filled glove box (O_2 and H_2O ≤0.5 ppm) with Li metal as the counter/reference electrode, and a polypropylene (PP, Celgard 2400, Celgard) film as the separator. The electrolyte solution contained 1 M $LiPF_6$ in a 1:1:1 (v/v) mixture of ethylene carbonate (EC), ethyl methyl carbonate (EMC) and dimethyl carbonate (DMC). Electrochemical characteristics of the batteries were measured with a multichannel potentiostat/galvanostat (WMPG 1000, WonATech, Korea) at room temperature. Galvanostatic charge-discharge cycles were characterized in the potential range of 1.0-3.0 V (vs Li/Li^+) at C-rate ranging from 0.5 to 40 C. Cyclic voltammetry (CV) was also conducted in the potential

range of 1.0-3.0 V at a scan rate of 0.1 mA s^{-1}. The electronic conductivity of the electrodes was evaluated in the frequency range between 100 kHz and 0.1 Hz using an AC voltage with an amplitude of 10 mV via electrochemical impedance spectroscopy (EIS, CHI6143E, CH Instruments, Inc., USA).

FIGURES

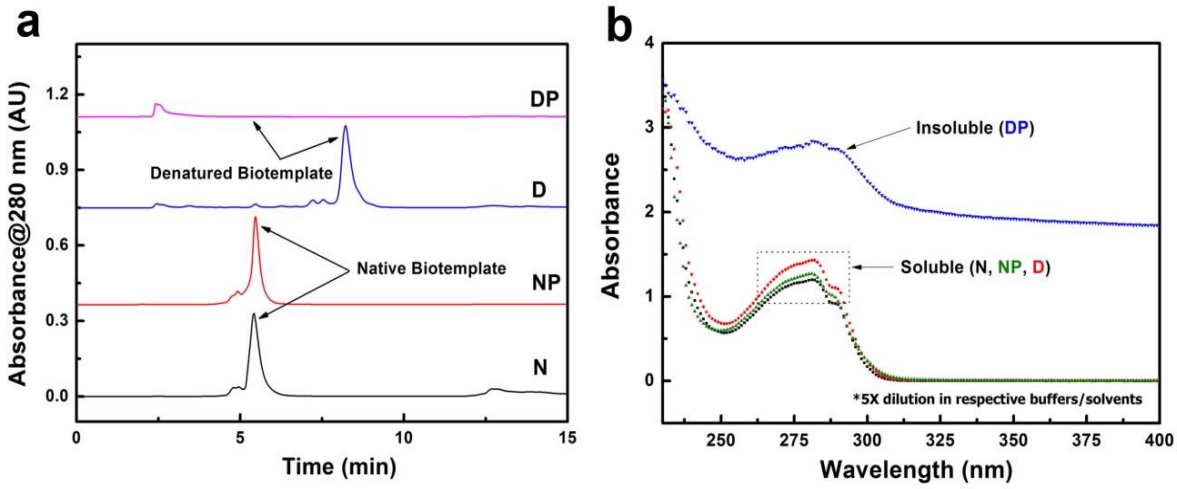

Figure S1. (a) RP-HPLC chromatogram, and (b) UV-Vis spectra of N, NP, D and DP biotemplates.

Explanation of Figure S1:

The retention peaks appearing near 5 and 8 min in Figure S1a indicate native (N and NP) and denatured lysozyme (D), respectively. There is no peak for DP as aggregated lysozyme particles could not pass through the 0.2 μm filter prior to the sample injection. In order to further investigate the protein structural changes, biotemplates were characterized using UV-Vis spectrophotometer in the wavelength range of 230-400 nm (Figure S1b). All solutions of soluble biotemplate (i.e., N, NP and D) were transparent and exhibited similar UV-Vis profiles. However, white precipitates were observed for DP due to the formation of insoluble lysozyme-phosphate complex. Hence, relatively greater absorbance in UV-Vis spectrum was observed for

the DP (Figure S1b), which is indicative of conformational changes via lysozyme-phosphate complex formation or lysozyme aggregation. In addition, to confirm the lysozyme aggregation by absorption spectroscopy, the turbidity of biotemplates was calculated using a relation of $\tau = (2.303 \times OD_{600})/l$, where l and OD_{600} are the width of the cuvette (i.e., 1 cm) and optical density at 600 nm wavelength, respectively. The turbidity values of native lysozyme were 0.064 and 0.056 cm^{-1} in the presence (NP) and absence of phosphate ions (N), respectively. In addition, denatured lysozyme (D) in water showed similar turbidity value near to 0.068 cm^{-1}, indicating that lysozyme was soluble and significant aggregate formation was not observed. In contrast, compared to the other biotemplates (N, NP and D), DP exhibited a high turbidity of 4.264 cm^{-1} due to the formation of insoluble lysozyme-phosphate complex.

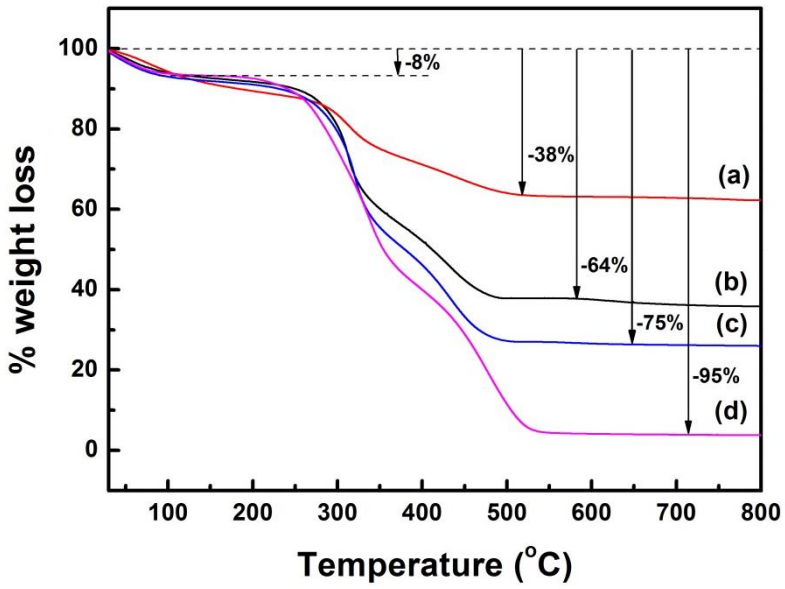

Figure S2. TGA of biomineralized TiO_2 particles (before calcination): (a) TNP, (b) TN, (c) TD and (d) TDP. The percentage of weight loss for each sample is indicated beside the drop-down arrow.

Explanation of Figure S2:

TGA analysis was used to characterize the organic biotemplate content of the biomineralized TiO_2 (Figure S2). As the biomineralized TiO_2 was heated from 25 to 800 °C, the weight loss increased with the increase in organic biotemplate content. At around 115 ^oC, surface adsorbed water molecules were removed and this constituted 8% weight loss in all samples. In addition, the significant weight loss that occurred between 300-520 ^oC for all samples could be attributed to the organic biotemplate content. The TGA profiles for all samples between 300-520 ^oC are distinctively different. The variation in the organic weight content among the biomineralized TiO_2 could be due to the incorporation of phosphate into the particles, and the state (i.e., native or denatured) of the biotemplate. There was no significant weight loss after 520 ^oC for all samples.

For particles from native biotemplate directed TiO_2 biomineralization, TN and TNP exhibit weight losses of 64 and 38%, respectively. The difference in the weight loss could be attributed to the incorporation of the phosphate ions from PB into TNP. This is accomplished via conjugation of lysozyme molecules with phosphate ions that leads to the formation of lysozyme-phosphate complex.[1] The use of lysozyme-phosphate biotemplate (i.e., NP) during biomineralization results in titanium phosphate formation in addition to TiO_2 formation. This increases the inorganic content compared to when N is used, and thus there is lower weight loss for TNP compared to TN.

For particles from denatured biotemplate directed TiO_2 biomineralization, TD and TDP exhibit weight losses of 75 and 95%, respectively. Despite the presence of lysozyme-phosphate complex and subsequent formation of additional titanium phosphate, TDP shows a higher weight loss than TD which is in contrast to the case for TNP vs TN. To explain this phenomenon, the structures of

the biotemplates have to be taken into account. DP is present in a hierarchical spherical structure consisting of lysozyme aggregates (ca. 1 μm) while D is present in a smaller aggregate cluster (ca. 0.5 μm) (Figure 1). The aggregation of lysozyme reduces the surface area available for interaction with TiBALDH precursor, and thus less TiO_2 are biomineralized. Hence, TDP with a higher degree of lysozyme aggregation possesses higher organic content than TD with a lower degree of lysozyme aggregation. In addition, TD biomineralized from denatured biotemplate D shows a higher weight loss compared to TN biomineralized from native biotemplate N. N does not have significant aggregation unlike D (Figure 1), and thus N has a higher surface area to interact with TiBALDH precursor to result in enhanced TiO_2 biomineralization. Hence, the amount of TiO_2 biomineralized by native biotemplate is higher than that of denatured biotemplate on a per lysozyme particle basis.

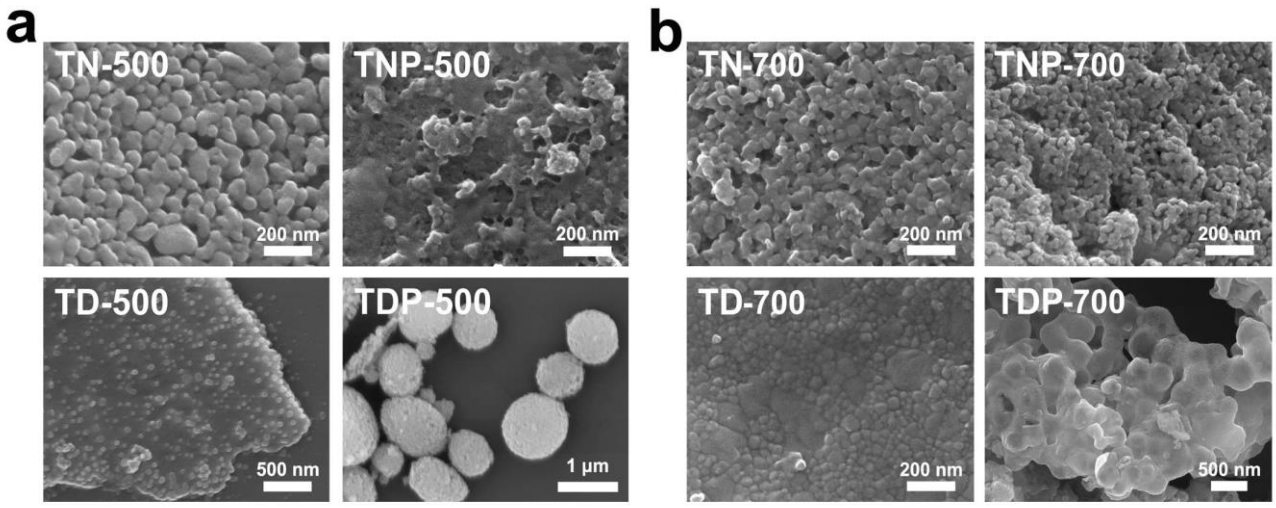

Figure S3. SEM images of TiO_2 particles calcined at (a) 500 (TN-500, TNP-500, TD-500, TDP-500), and (b) 700 ^{o}C (TN-700, TNP-700, TD-700, TDP-700).

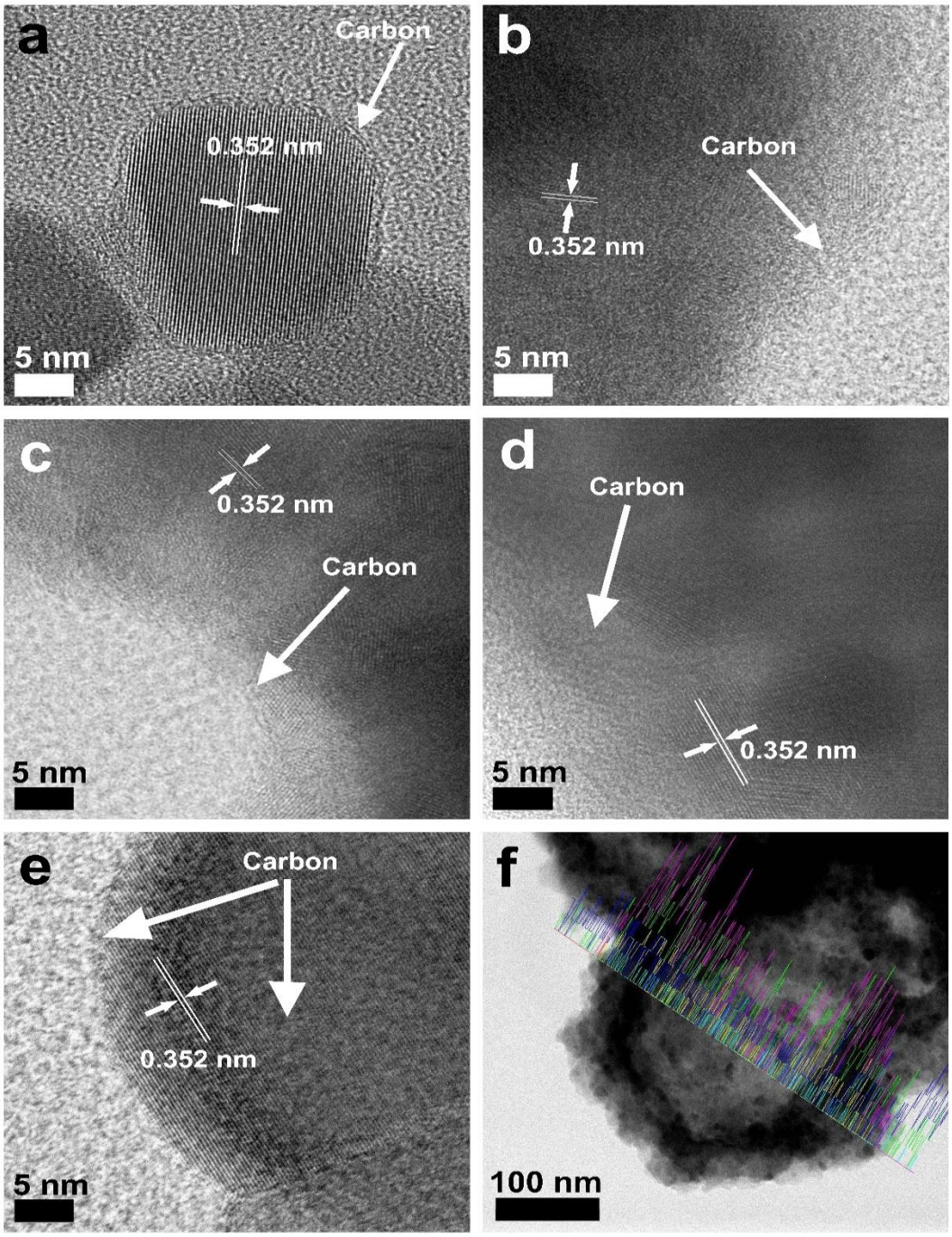

Figure S4. HRTEM images of (a) TNP-700, (b) TDP-600, (c) TDP-700, (d) TDP-800 and (e) TDP-900. (f) TEM image of TDP-700 with EDX mapping of Ti (Pink), P (Yellow), C (Blue) and O (Green). The EDX for TDP-500 is similar to TDP-700, and thus not shown.

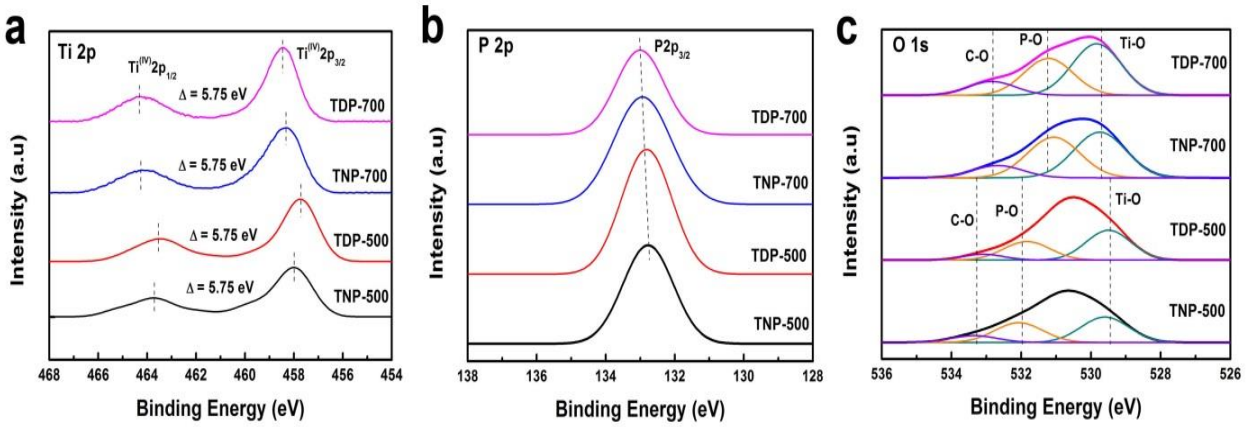

Figure S5. High-resolution XPS spectra of (a) Ti 2p, (b) P 2p, and (c) O 1s for TNP-500, TNP-700, TDP-500 and TDP-700.

Explanation of Figure S5:

The presence of titanium in TNP-500, TNP-700, TDP-500 and TDP-700 is confirmed by the high-resolution Ti 2p XPS spectra (Figure S5a). The two characteristic peaks of Ti^{4+} $2p_{3/2}$ and Ti^{4+} $2p_{1/2}$ centered at ca. 458 eV and 464 eV, respectively, indicate the existence of Ti^{4+} state. The presence of phosphorus in calcined TNP and TDP is ascertained through the high-resolution P 2p XPS spectrum (Figure S5b). The BE peak of ca. 133 eV indicates that phosphorus is in a P^{5+} state, whereas the absence of BE peak at ca. 129 eV indicates that P^{3-} state is not present which rules out the existence of Ti-P bonds.[2] The ionic radii of P^{5+} ca. 0.38 Å and Ti^{4+} ca. 0.67 Å suggest that P^{5+} can enter into Ti^{4+} sites in the crystal lattice of TiO_2 by formation of Ti-O-P bonds.[3] The high-resolution O 1s spectra (Figure S5c) can be fitted by three peaks, C-O bond, Ti-O bond and P-O bond, which further support the presence of Ti-O-P bonds in TNP and TDP. For TNP-700 and TDP-700, the BE peak for P-O was slightly enhanced and blue shifted as compared to TNP-500 and TDP-500. This could be due to the structural changes and/or rearrangements upon calcination of the samples at higher temperature of 700 ^{o}C. It should be noted that calcined TN and TD samples do not show any phosphorus signal (data not shown).

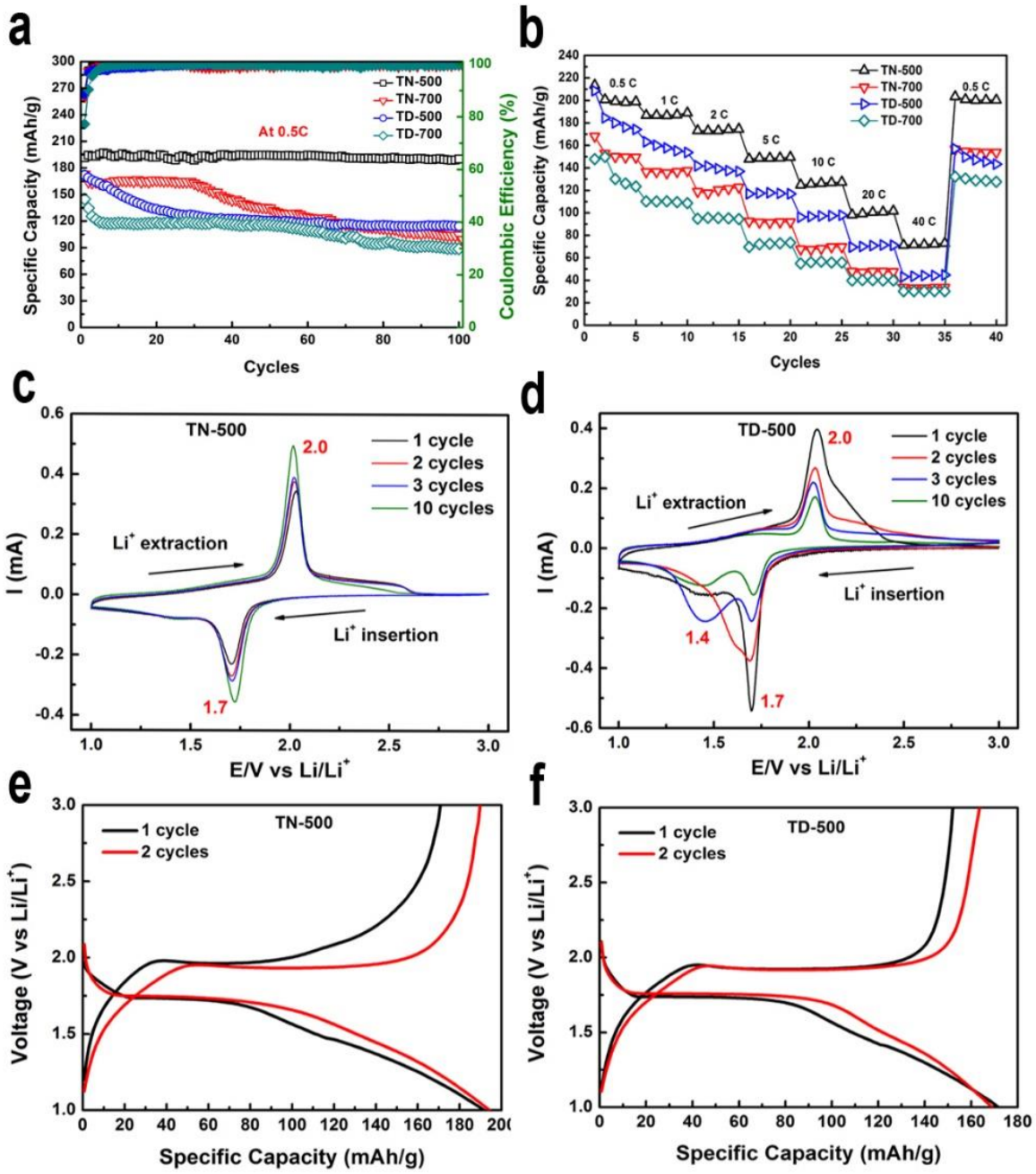

Figure S6. Electrochemical performances of TiO_2 particles as anodes: (a) Cycling performance of TN-500, TN-700, TD-500 and TD-700 for 100 cycles at 0.5 C, (b) Rate capabilities of TN-500, TN-700, TD-500 and TD-700 at 0.5, 1, 2, 5, 10, 20 and 40 C, CV of (c) TN-500 and (d) TD-500, and Galvanostatic charge-discharge profiles of (e) TN-500, and (f) TD-500 in the potential range of 1.0-3.0 V (vs Li/Li^+) at a rate of 0.5 C.

Explanation of Figure S6:

The estimation of the capacity retention (calculated from differences between the 1st and 100th discharge cycles) of TN-500, TD-500, TN-700 and TD-700 was ca. 99, 53, 57 and 61%, respectively (Figure S6a). TN-500 exhibits the highest capacity retention at ca. 99%. In addition, the rate capabilities of all the calcined TN and TD samples were also investigated at C-rates ranging from 0.5 to 40 C (Figure S6b), and are presented in Table 3. From the rate capability results of TN and TD (Figure S6b and Table 3), it can be stated that the performance of TN-500 at all C-rates (with higher specific capacity and retention % of specific capacity) is better than TD-500. The higher rate capability of TN-500 is mainly due to its morphology with distinct interconnected particles, meso-macroporous structure (both of which not present in TD-500) and higher specific pore volume of 0.59 $cm^3\ g^{-1}$ as compared to TD-500 (0.40 $cm^3\ g^{-1}$) (Table 2). However, when TN and TD were calcined at 700 ^oC, the performance of TN-700 at all C-rates (with slightly higher or similar specific capacity and retention (%) in specific capacity) is only slightly better or similar to TD-700 (Figure S6b and Table 3). This could be due to the presence of anatase-rutile mixed phases, similar mesopore sizes and/or structures, and anatase grain sizes for both TN-700 and TD-700 (Tables 1 and 2).

Next, the electrochemical characteristics of the two better performers (i.e., TN-500 with native template, and TD-500 with denatured template) during Li^+ insertion/extraction were elucidated by CV (at a scan rate of 0.1 mV s^{-1}) and compared (Figures S6c and d). The two redox peaks at ca. 2.0 (oxidation) and 1.7 V (reduction) are associated with the delithiation and lithiation in anatase TiO_2, respectively.[4-5] Next, galvanostatic charge-discharge profiles (first two cycles) of TN-500 and TD-500 (Figures S6e and f) were investigated at 0.5 C in the voltage range between 1.0 and 3.0 V (vs Li^+/Li). In the first discharge curve (i.e., lithiation of TN-500 and TD-500), the

initial rapid voltage drop from 3.0 to 1.7 V corresponds to the formation of the conductive solid-solution Li_xTiO_2 where TiO_2 phase remains unmodified. The subsequent voltage plateau at 1.7 V is associated with the phase transition from TiO_2 to Li_xTiO_2, which is in good agreement with the reduction peak in the CV profile (Figures S6c and d). Following which, the gradual decrease in voltage between 1.7 and 1.0 V (Figures S6e and f) indicates the accumulation of Li^+ ion at the solid-liquid interface. In the first charge curve (i.e., delithiation of TN-500 and TD-500), the rapid voltage increase from 1.0 to 2.0 V (Figures S6e and f) corresponds to disruption of Li_xTiO_2 phase to form conductive solid-solution Li_xTiO_2. The subsequent voltage plateau at 2.0 V is associated with the phase transition from Li_xTiO_2 to TiO_2, which is in good agreement with oxidation peak in the CV profile (Figures S6c and d).[4] Subsequently, the sharp increase in voltage between 2.0 to 3.0 V (Figure S6e and f) corresponds to the stage where the electrochemical reaction of the electrode is reversed.[6] Although TN and TD have similar crystalline phases, TN-500 exhibits better reproducibility in I-V characteristics (Figures S6c and d) and stability for short-term cycling (i.e., 100 cycles) (Figure S6a) as compared to TD-500. The performance of TD-500 deteriorates during repeated lithiation/delithiation processes (Figure S6c), and a reduction peak of ca. 1.4 V starts to appear from the 3rd cycle onward (Figure S6d). This is presumably due to the difference in structural arrangement of TiO_2 crystal lattice in TD-500.[7] Further insight into the structural differences and their effect on CV peaks are not taken into consideration in the present work.

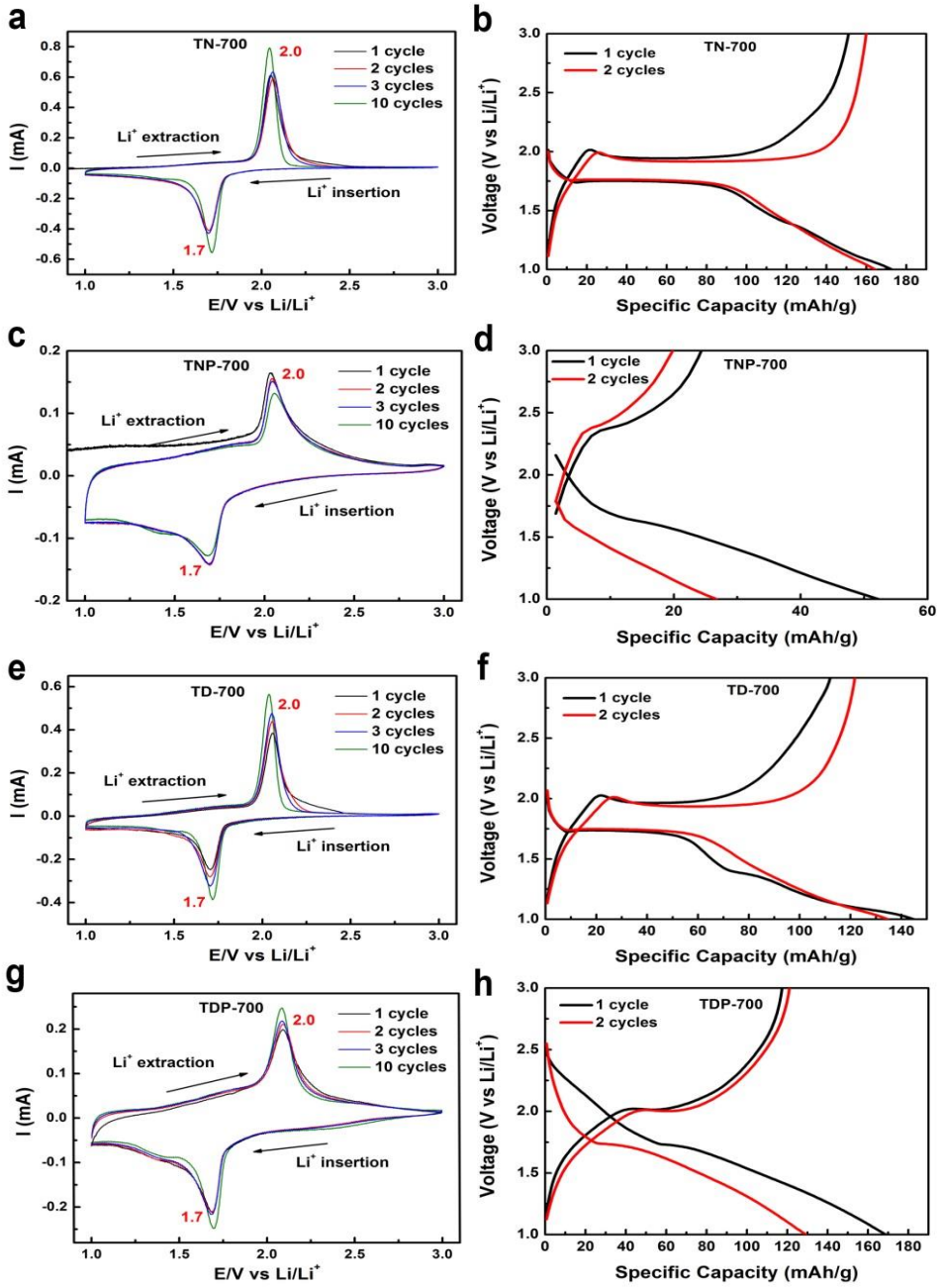

Figure S7. CV and charge-discharge profiles of (a, b) TN-700, (c, d) TNP-700, (e, f) TD-700, and (g, h) TDP-700 in the potential range of 1.0-3.0 V (vs Li/Li^+) at a rate of 0.5 C.

TABLE(S)

Table S1. Electrochemical performance of TiO_2-based anodes for Li-ion battery as compared to TiO_2 particles synthesized in the present work.

Material	Process	Specific capacity (mA h g^{-1})	Capacity retention (%)	Rate capability (mA h g^{-1})	Ref
Mesoporous TiO_2 nanocrystalline	Sol-gel	163 after 10 cycles at 0.2 C	89.6	84 at 10 C 67 at 20 C	[8]
TiO_2 hollow structures	Shape-controlled synthesis using Fe_2O_3 particles	122 after 30 cycles at 0.2 C	77.7		[9]
Porous TiO_2	Yeast bio-template synthesis	255.98 after 100 cycles at 0.7 C	80	112.93 at 10 C 84.65 at 20 C	[10]
Porous TiO_2 spheres	Microwave assisted sol-gel synthesis	176 after 100 cycles at 0.7 C	92	119 at 5 C	[11]
Hollow TiO_{2-x} porous microspheres (where x indicates after hydrogenation treatment)	Sol-gel template-assisted approach	151 after 300 cycles at 1 C	81.6	171 at 0.5 C 127 at 1 C 71 at 5 C 42.5 at 10 C	[12]
Meso-macroporous TiO_2 particles (TN-500)	Native lysozyme mediated synthesis in water	190 after 100 cycles at 0.5 C	99	186 at 1 C 150 at 5 C 100 at 20 C 72 at 40 C	Present work
Meso-macroporous hollow TiO_2 spheres (TDP-500)	Denatured lysozyme-mediated synthesis in PB	147 after 100 cycles at 0.5 C	91	146 at 1 C 130 at 5 C 115 at 20 C 103 at 40 C	Present work

REFERENCES

1. Choi, N.; Tan, L.; Jang, J.-r.; Um, Y. M.; Yoo, P. J.; Choe, W.-S. The interplay of peptide sequence and local structure in TiO_2 biomineralization. *J. Inorg. Biochem.* **2012,** *115*, 20-27.
2. Yu, J. C.; Zhang, L.; Zheng, Z.; Zhao, J. Synthesis and Characterization of Phosphated Mesoporous Titanium Dioxide with High Photocatalytic Activity. *Chem. Mater.* **2003,** *15*, 2280-2286.
3. Sotelo-Vazquez, C.; Noor, N.; Kafizas, A.; Quesada-Cabrera, R.; Scanlon, D. O.; Taylor, A.; Durrant, J. R.; Parkin, I. P. Multifunctional P-Doped TiO_2 Films: A New Approach to Self-Cleaning, Transparent Conducting Oxide Materials. *Chem. Mater.* **2015,** *27*, 3234-3242.
4. Zhang, X.; Suresh Kumar, P.; Aravindan, V.; Liu, H. H.; Sundaramurthy, J.; Mhaisalkar, S. G.; Duong, H. M.; Ramakrishna, S.; Madhavi, S. Electrospun TiO_2–Graphene Composite Nanofibers as a Highly Durable Insertion Anode for Lithium Ion Batteries. *J. Phys. Chem. C* **2012,** *116*, 14780-14788.
5. Li, X.; Zhang, C.; Meng, T. Synergistic effects from graphene oxide nanosheets and TiO_2 hierarchical structures enable robust and resilient electrodes for high-performance lithium-ion batteries. *RSC Adv.* **2016,** *6*, 4321-4328.
6. Liu, C.; Neale, Z. G.; Cao, G. Understanding electrochemical potentials of cathode materials in rechargeable batteries. *Mater. Today* **2016,** *19*, 109-123.
7. Brumbarov, J.; Vivek, J. P.; Leonardi, S.; Valero-Vidal, C.; Portenkirchner, E.; Kunze-Liebhauser, J. Oxygen deficient, carbon coated self-organized TiO_2 nanotubes as anode material for Li-ion intercalation. *J. Mater. Chem. A* **2015,** *3*, 16469-16477.

8. Casino, S.; Di Lupo, F.; Francia, C.; Tuel, A.; Bodoardo, S.; Gerbaldi, C. Surfactant-assisted sol gel preparation of high-surface area mesoporous TiO_2 nanocrystalline Li-ion battery anodes. *J. Alloys Compd.* **2014,** *594*, 114-121.
9. Wang, Y.; Su, X.; Lu, S. Shape-controlled synthesis of TiO_2 hollow structures and their application in lithium batteries. *J. Mater. Chem.* **2012,** *22*, 1969-1976.
10. Li, Y.-N.; Su, J.; Lv, X.-Y.; Long, Y.-F.; Wen, Y.-X. Yeast bio-template synthesis of porous anatase TiO_2 and potential application as an anode for sodium-ion batteries. *Electrochim. Acta* **2015,** *182*, 596-603.
11. Wang, H.-E.; Jin, J.; Cai, Y.; Xu, J.-M.; Chen, D.-S.; Zheng, X.-F.; Deng, Z.; Li, Y.; Bello, I.; Su, B.-L. Facile and fast synthesis of porous TiO_2 spheres for use in lithium ion batteries. *J. Colloid Interface Sci.* **2014,** *417*, 144-151.
12. Wang, C.; Wang, F.; Zhao, Y.; Li, Y.; Yue, Q.; Liu, Y.; Liu, Y.; Elzatahry, A. A.; Al-Enizi, A.; Wu, Y.; Deng, Y.; Zhao, D. Hollow TiO_{2-X} porous microspheres composed of well-crystalline nanocrystals for high-performance lithium-ion batteries. *Nano Res.* **2016,** *9*, 165-173.